

## The Herschel PACS photometer calibration

### A time dependent flux calibration for the PACS chopped point-source photometry AOT mode

Markus Nielbock · Thomas Müller · Ulrich  
Klaas · Bruno Altieri · Zoltán Balog · Nicolas  
Billot · Hendrik Linz · Koryo Okumura ·  
Miguel Sánchez-Portal · Marc Sauvage

Received: date / Accepted: date

**Abstract** We present a flux calibration scheme for the PACS chopped point-source photometry observing mode based on the photometry of five stellar standard sources. This mode was used for science observations only early in the mission. Later, it was only used for pointing and flux calibration measurements. Its calibration turns this type of observation into fully validated data products in the Herschel Science Archive. Systematic differences in calibration with regard to the principal photometer observation mode, the scan map, are derived and amount to 5 – 6%. An empirical method to calibrate out an apparent response drift during the first 300 Operational Days is presented. The relative photometric calibration accuracy (repeatability) is as good as 1% in the blue and green band and up to 5% in the red band. Like for the scan map mode, inconsistencies among the stellar calibration models become visible and amount to 2% for the five standard stars used. The absolute calibration accuracy is therefore mainly limited by the model uncertainty, which is 5% for all three bands.

**Keywords** Herschel Space Observatory · PACS · Far-infrared · Instrumentation · Calibration · Chopping

---

M. Nielbock, Z. Balog, U. Klaas, H. Linz  
Max-Planck-Institut für Astronomie, Königstuhl 17, D-69117 Heidelberg, Germany  
Tel.: +49 6221 528-445  
E-mail: nielbock@mpia.de

B. Altieri, M. Sánchez-Portal  
European Space Astronomy Centre (ESAC)/ESA, Villanueva de la Cañada, E-28691 Madrid, Spain

N. Billot  
Instituto de Radio Astronomía Milimétrica, Avenida Divina Pastora, 7, Local 20, 18012 Granada, Spain

Th. Müller  
Max-Planck-Institut für extraterrestrische Physik, Gießenbachstraße, D-85741 Garching, Germany

K. Okumura, M. Sauvage  
Laboratoire AIM, CEA, Université Paris Diderot, IRFU/Service d’Astrophysique, Bat. 709, 91191 Gif-sur-Yvette, France

**Table 1** Specifications of the five prime flux standards used for calibrating the PACS photometer response.

ID	HIP	ICRS coordinates (J2000)		Spectral Type	Model flux [mJy]		
		RA	Dec		70 $\mu\text{m}$	100 $\mu\text{m}$	160 $\mu\text{m}$
$\alpha$ Boo	69673	14:15:39.67207	+19:10:56.6730	K1.5III	15434	7509	2891
$\alpha$ Cet	14135	03:02:16.77307	+04:05:23.0596	M1.5IIIa	4889	2393	928
$\alpha$ Tau	21421	04:35:55.23907	+16:30:33.4885	K5III	14131	6909	2677
$\beta$ And	5447	01:09:43.92388	+35:37:14.0075	M0III	5594	2737	1062
$\gamma$ Dra	87833	17:56:36.36988	+51:29:20.0242	K5III	3283	1604	621

**Note.** The coordinates are taken from [13]. The model fluxes are based on [2].

## 1 Introduction

The Photodetector Array Camera and Spectrograph (PACS<sup>1</sup>) [11] on board the Herschel Space Observatory [10] provides photometric imaging and integral field spectroscopy capabilities for the far-infrared (FIR) wavelength regime. The PACS photometer unit is a dual band imaging camera. It permits the simultaneous observation in two bands, either in the combination 70  $\mu\text{m}$ /160  $\mu\text{m}$  or 100  $\mu\text{m}$ /160  $\mu\text{m}$ , where 70 or 100  $\mu\text{m}$  bands are selected by a filter wheel. The camera contains two bolometer detector arrays with  $64 \times 32$  pixels (blue array) and  $32 \times 16$  pixels (red array) providing an instantaneous field-of-view of  $3'.5 \times 1'.75$ . The detector arrays are made of 8 and 2 filled bolometer matrices with  $16 \times 16$  pixels each, respectively. They operate at  $\sim 285$  mK provided by a <sup>3</sup>He sorption cooler with a hold time of 57.8 h, if the bolometers are biased all the time after the cooler recycling.

While the principal science observation mode with the PACS photometer is the scan map with the telescope scanning along parallel legs covering the map area<sup>2</sup>, another photometer observing mode was maintained throughout the mission: the chopped point-source photometry Astronomical Observing Template (AOT)<sup>3</sup>. For a general description of the differential measurement technique by chopping, see [3]. The chopping technique has been used in space-borne FIR instrumentation like ISOPHOT [6] and ground-based mid-infrared cameras like TIMMI2 [12] and VISIR [5]. Inside PACS, it is achieved by using the instrument internal focal plane chopper to provide signal modulation by on-array chopping (see Fig. 1). This restricts the useful field-of-view to roughly  $50''$ , hence is only useful for point or very compact source photometry. It was used for science observations early in the mission and later only as calibration mode for

1. Observatory pointing calibration, which allowed a more accurate source position determination than scan mapping,

<sup>1</sup> PACS has been developed by a consortium of institutes led by MPE (Germany) and including UVIE (Austria); KU Leuven, CSL, IMEC (Belgium); CEA, LAM (France); MPIA (Germany); INAF-IFSI/OAA/OAP/OAT, LENS, SISSA (Italy); IAC (Spain). This development has been supported by the funding agencies BMVIT (Austria), ESA-PRODEX (Belgium), CEA/CNES (France), DLR (Germany), ASI/INAF (Italy), and CICYT/MCYT (Spain).

<sup>2</sup> [http://herschel.esac.esa.int/Docs/PACS/html/pacs\\_om.html](http://herschel.esac.esa.int/Docs/PACS/html/pacs_om.html)

<sup>3</sup> [http://herschel.esac.esa.int/twiki/pub/Public/PacsCalibrationWeb/PhotMiniScan\\_ReleaseNote\\_20101112.pdf](http://herschel.esac.esa.int/twiki/pub/Public/PacsCalibrationWeb/PhotMiniScan_ReleaseNote_20101112.pdf)

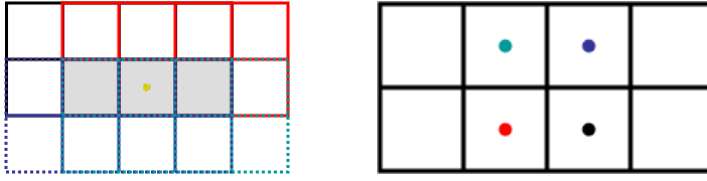


**Fig. 1** Illustration of the detector footprint of the blue detector array on the sky (left) and the chop-nod source pattern (right) produced on the detector during the execution of the point-source photometry AOT that offsets the observed direction by about  $50''$  in perpendicular directions, both for chopping and nodding. The colours reflect the four combinations of the nodding and chopping positions attained during the observing sequence: ● nod 1 chop A, ● nod 1 chop B, ● nod 2 chop A, ● nod 2 chop B. The detector array with a field-of-view of  $3'.5 \times 1'.75$  consists of eight individual sub-matrices.

2. a low cost independent flux calibration check on the same celestial standards as used for the scan map calibration.

In total, 2200 observations that sum up to 200 hours of Herschel observing time have been executed in this mode, adding a wealth of astronomical data to the Herschel Science Archive (HSA). 16 hours are from scientific observing programmes, while 184 hours are spent on calibration observations of point sources like stars, asteroids and planets. It is therefore the intention of this paper to make this type of observation fully validated data products by providing a consistent flux calibration scheme. For an overview of the basic calibration strategy we refer to the analogous steps of the scan map flux calibration [1]. Here we concentrate on working out and characterising the specific properties of this mode.

## 2 Observations

Altogether, 137 observations (see Tab. 6) of the five PACS prime standard stars (see Tab. 1) were obtained using the chopped point-source photometry AOT. The stellar models<sup>4</sup> are based on [2]. For a more detailed discussion see [1]. In the case of PACS, chopping is done with a focal plane chopping mirror [4] operating at a frequency of 1.25 Hz that produces a displacement of  $\sim 50''$  on the sky along the detector y-axis. Synchronised with the chopper movement, the data are read out with a rate of 40 Hz, but averaged to a 10 Hz resolution on board (see Fig. 2). Nodding is achieved by offsetting the telescope by the same amount along the detector z-axis. On each nod-position, the chopper executes  $3 \times 25$  cycles. The three sets of chopping cycles are either on the same array position (no dithering) or on 3 different array positions (dither option). If dithering is applied, the chopper pattern is displaced by  $2 \frac{2}{3}$  blue or by  $1 \frac{1}{3}$  red detector pixels along the detector y-axis. The detector footprint on sky without dithering as well as the resulting target pattern on the detector is shown in Fig. 1. For details see the PACS Observer's Manual<sup>5</sup>. The observation of the science target is always preceded by a chopped measurement on the internal calibration sources, known as the calibration block, or brief, calblock. This information

<sup>4</sup> Model spectra are available at: <ftp://ftp.ster.kuleuven.be/dist/pacs/calsources>

<sup>5</sup> [http://herschel.esac.esa.int/Docs/PACS/html/pacs\\_om.html](http://herschel.esac.esa.int/Docs/PACS/html/pacs_om.html)

**Table 2** Numbers of observations per object and spectral band.  $\gamma$  Dra is the designated response stability monitoring target. Thus, it was observed more frequently than the other four objects.

Object	70 $\mu$ m	100 $\mu$ m	160 $\mu$ m
$\alpha$ Boo	8	7	15
$\alpha$ Cet	10	7	17
$\alpha$ Tau	13	10	23
$\beta$ And	6	6	12
$\gamma$ Dra	61	9	70

is not used for calibrating the detector response drifts during processing, but serves as a basis for long term trend corrections. A detailed analysis is given in [7].

The observations were always set up in a very similar manner, e. g. fixed to a single repetition which leads to identical on-target times of 124 s and a duration of 152 s for the Astronomical Observing Request (AOR) including overheads but omitting the initial slew. Apart from two exceptional cases, dithering was used. However, we did not see any significant difference in terms of measured target flux. The gain parameter was set to “high” for nearly all observations. However, changing the gain parameter has no influence on the photometry of the selected targets. The number of observations per object and spectral band is given in Tab. 2.

Please note that on operational day (OD) 1375, one of the two red detector matrices failed and never recovered. As of PACS calibration version<sup>6</sup> 48, this unusable matrix is flagged automatically during the data processing. As a result, all observations at 160  $\mu$ m obtained since then are affected by a reduced spatial coverage and consequently by a degraded sensitivity.

### 3 Data processing

The data have been processed in a straightforward manner that is effectively very similar to the standard pipeline<sup>7</sup> [14] (version 9.1 and later) provided by the Herschel Science Centre (HSC) of the European Space Agency (ESA) via the HSA. In particular, it comprises

- flagging of outliers (bad pixels, electronic saturation and crosstalk, data recorded during chopper transitions)
- averaging data per chopper plateau (first readout is discarded due to slow detector response)
- producing differential signals per chop cycle
- response calibration and flat fielding
- sorting for and averaging per dither position
- deglitching via sigma clipping algorithm
- averaging data per nod position and subtracting
- producing map via shift-and-add algorithm

<sup>6</sup> <http://herschel.esac.esa.int/twiki/bin/view/Public/PacsCalTreeHistory>

<sup>7</sup> [http://herschel.esac.esa.int/hcss-doc-10.0/index.jsp#pacs\\_phot:PdrgP.Chp.3.chopnod](http://herschel.esac.esa.int/hcss-doc-10.0/index.jsp#pacs_phot:PdrgP.Chp.3.chopnod)

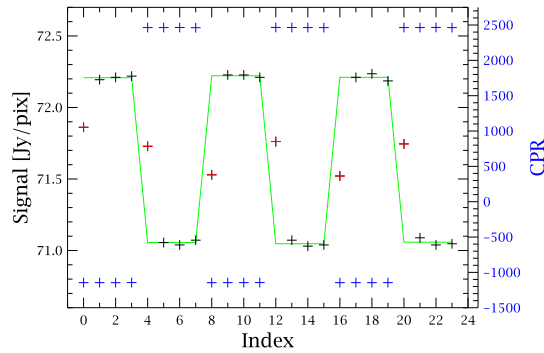


**Fig. 2** Detailed view of the detector signals for a single bolometer pixel during a sequence of three chopping cycles. The detector signals are in black, the averaged value per chopper plateau is shown as a green line. The red crosses denote detector signals that have been discarded. Although the chopper reaches the commanded position (blue crosses, in digital readout units), the first detector signal of a chopper plateau is too low due to the inertia of the response.

The first two steps are visualised in Fig. 2. The blue crosses show how the chopper position alternates between two values given in digital readout units. The red and black crosses represent the detector signal measured at those chopper positions. The first readout obtained at a new chopper position does not provide the true full signal (red crosses) due to a detector response lag phenomenon. Therefore, those data are flagged and removed from the subsequent processing. The green line depicts the detector signal after averaging over a given chopper plateau.

The unreleased PACS calibration version 53 was used, which for most PACS photometer aspects is identical to versions 41 (SPG 9.1) and 48 (SPG 10), which is the latest publicly released version. Therefore, the calibration set is almost identical to what was used for the Standard Pipeline Generation (SPG). In particular, the standard response calibration (FM,7) was applied which is based on scan map observations of the five prime calibration stars.

In addition, we have included an updated detector pixel table containing the corner positions for each pixel, which reflects the optical distortions on the sky. Another improvement is a correction for response changes that are caused by temperature variations of the bolometer  $^3\text{He}$  cooler [1, 7]. For the dataset presented here, the correction changes the flux levels by  $(+0.6 \pm 0.6)\%$  at  $70 \mu\text{m}$ ,  $(+0.7 \pm 0.8)\%$  at  $100 \mu\text{m}$ , and  $(+0.5 \pm 0.5)\%$  at  $160 \mu\text{m}$ . Those corrections will be made available in future releases of the Herschel Interactive Processing Environment (HIPE) [9]. A non-linearity correction was not necessary, because all the five standard stars are too faint to cause any detector non-linearity effects. The thresholds of non-linearity effects caused by point source fluxes are approximately 50, 70, and 40 Jy at 70, 100, and 160  $\mu\text{m}$ , respectively.

We have also used corrected pointing products as provided by the HSC<sup>8</sup>. They provide focal length field distortion corrections of the star tracker camera for ODs 320 until 761 and hence improve the telescope pointing information during data process-

<sup>8</sup> <http://herschel.esac.esa.int/twiki/bin/view/Public/HowToUseImprovedPointingProducts>

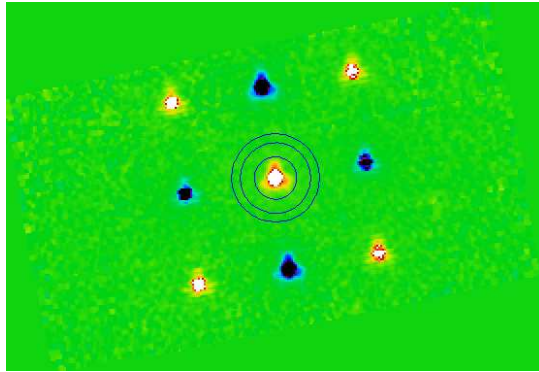


**Fig. 3** Point-source map of  $\gamma$  Dra obtained at  $70 \mu\text{m}$ . It is produced by a shift-and-add technique that co-adds the four images of the source that are produced by the chop-nod observing method (see Fig. 1). As a result, only the central image of the nine must be used for photometry and further analysis. The triangular shape of the source reflects the typical PSF of a point source. The aperture ( $12''$ ) and sky annulus used for the photometry are superimposed. The FOV of the co-added map is  $4'.7 \times 2'.7$ , but the useful area of the central target image is given by the chop and the nod throw, i.e. approximately  $50''$ .

ing. Revised pointing products for earlier ODs are not yet available. For observations obtained at later ODs, the correct focal length was used for the pointing calculations on-board.

We used a pixel scaling for creating the final point-source maps that differs from the SPG settings. It was chosen to appropriately sample the target point spread function (PSF) by covering the nominal full width at half maximum (FWHM) with five map pixels. The resulting map pixel scales are  $1''.1$ ,  $1''.4$ , and  $2''.1$  at  $70$ ,  $100$ , and  $160 \mu\text{m}$ , respectively.

#### 4 Photometry

The `annularSkyAperturePhotometry` task of HIPE was used to determine the source flux from the point-source map that is produced by applying a shift-and-add algorithm. For observations obtained at  $70$  and  $100 \mu\text{m}$ , we set the aperture radius to  $12''$ , the inner sky annulus to  $20''$  and the outer sky annulus to  $25''$ . For observations in the  $160 \mu\text{m}$  band, we selected an aperture radius of  $22''$ , while the sky annulus ranged from  $24''$  to  $28''$ . The maximum radius is constrained by the size of the inner patch of the final map (Fig. 3) that contains the actual photometric information. The sky range was only used to estimate the photometric uncertainty. A background offset was not subtracted, because the chop-nod observing technique already provides background subtracted maps for single and isolated point-sources. We set the option `centroid` to `false` and extracted the central source positions from 2D Gaussian fits beforehand that were fed into the photometry algorithm.

An aperture correction was applied to account for the point-source flux outside the aperture via the `photApertureCorrectionPointSource` task. It is strictly only valid for scan map observations that produce PSFs that are slightly different from the chop-nod observations. However, the apertures are chosen large enough so that the

**Table 3** Results of the photometry of the five prime standard stars. The quoted numbers are the mean values of the flux ratios from OD 300 onwards. When combining more than one object, the mean is weighted by the number of objects.

Object(s)	70 $\mu\text{m}$	$\langle F_{\text{obs}}/F_{\text{model}} \rangle_{\geq \text{OD } 300}$ 100 $\mu\text{m}$	160 $\mu\text{m}$
$\alpha$ Boo	$0.928 \pm 0.011$	$0.942 \pm 0.005$	$0.958 \pm 0.009$
$\alpha$ Cet	$0.949 \pm 0.006$	$0.956 \pm 0.006$	$0.991 \pm 0.031$
$\alpha$ Tau	$0.912 \pm 0.008$	$0.926 \pm 0.006$	$0.933 \pm 0.011$
$\beta$ And	$0.959 \pm 0.011$	$0.966 \pm 0.004$	$0.938 \pm 0.012$
$\gamma$ Dra	$0.927 \pm 0.009$	$0.931 \pm 0.007$	$0.948 \pm 0.046$
K giants	$0.922 \pm 0.009$	$0.933 \pm 0.008$	$0.946 \pm 0.013$
M giants	$0.954 \pm 0.007$	$0.961 \pm 0.007$	$0.965 \pm 0.037$
all	$0.935 \pm 0.019$	$0.944 \pm 0.017$	$0.954 \pm 0.023$

differences are insignificant and the source flux is reliably recovered. The correction factors by which the measured point source fluxes are divided are 0.802, 0.776, and 0.817 at 70, 100, and 160  $\mu\text{m}$ , respectively.

The colour correction values for the fiducial stars (1.016, 1.033, 1.074) were derived from a 4000 K black body. We repeated now the calculation using the official model template files (see Sect. 2) and could confirm the tabulated values in the blue and red band. In the green band we found a difference of 0.1% (1.034) when using the full stellar templates instead of a 4000 K black body. No difference between the K and M-giants are seen on the per mille level. In the final error budget, this small deviation can be neglected and the colour correction is not contributing to the systematic differences between K and M-giants seen in the calibrated flux densities of the 5 fiducial stars.

The photometric results obtained from the three PACS bands are given in Fig. 4. For comparison, we show the ratios between the modelled and observed source fluxes (see Tab. 1). The error bars represent the photometric uncertainties as they are calculated by the aperture photometry algorithm. Note that the true photometric uncertainties can be considerably higher, because the maps suffer from correlated noise. Empirical investigations imply that for the chosen pixel sizes the true photometric uncertainty can be higher by up to a factor of 6, 4, and 8 at 70, 100, and 160  $\mu\text{m}$ , respectively. For the time scale, we provide both the elapsed time since launch as ODs and the Herschel internal canonical `FineTime` format as microseconds elapsed since 1 January 1958<sup>9</sup>. For the subsequent analysis, we only use `FineTime`, because the ODs have variable lengths.

## 5 Results

Several results are obvious from the measurements presented in Fig. 4.

1. There is an initial decline in response visible until OD 300, most obviously witnessed in the 70  $\mu\text{m}$  band.

<sup>9</sup> This is the defined zero point of the International Atomic Time (TAI) standard.

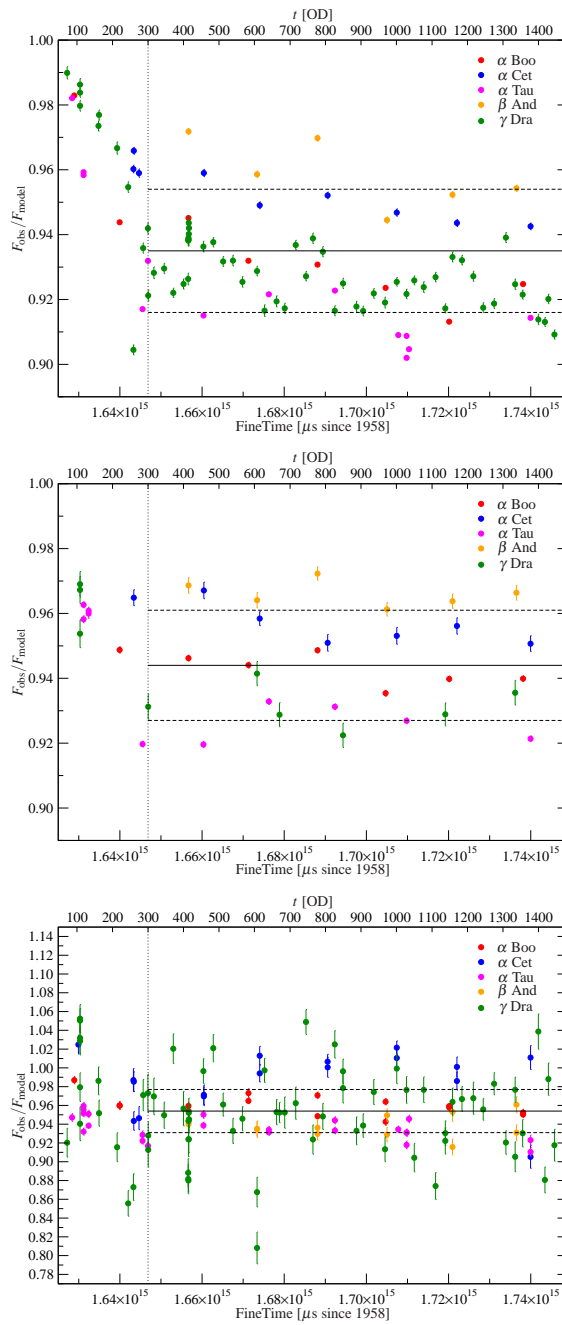


**Fig. 4** Photometric results of the stellar calibration sources at 70, 100, and 160  $\mu\text{m}$  (top to bottom) vs. time. The time scales are given in `FineTime` units, i. e. microseconds since 1 January 1958, and in operational days (OD) since launch. The flux scale is given in ratios between the model and the observed source fluxes. The horizontal lines depict the mean and the rms of the averaged photometric results for  $\text{OD} \geq 300$  obtained for the three wave bands.



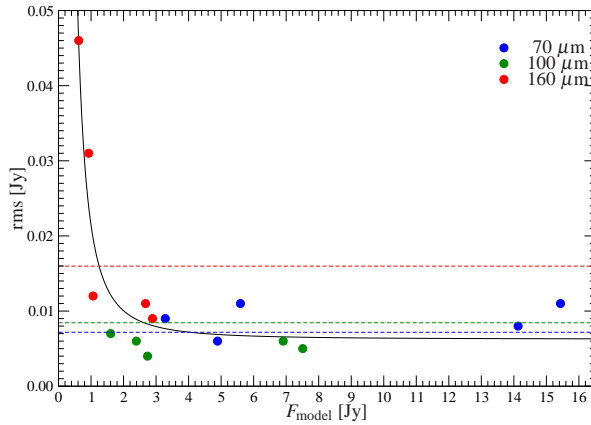


**Fig. 5** Relation between the rms of the photometry for the individual objects and their model flux in the three filter bands. The solid black line is a fit to the data according to  $\text{rms} = c_1 \cdot F_{\text{model}}^{-2} + c_2$ . The dashed horizontal lines represent the expected photometric uncertainties at the corresponding three wave bands as predicted by the HSPOT observing planning tool.

2. After OD 300, the flux ratios remain fairly constant.
3. There is an apparent offset between the K giant stars ( $\alpha$  Boo,  $\alpha$  Tau,  $\gamma$  Dra) and the M giant stars ( $\alpha$  Cet,  $\beta$  And) at 70  $\mu\text{m}$  and 100  $\mu\text{m}$  of about 3%, which is pointing to systematic uncertainties in the underlying stellar models that are quoted to be accurate to 5% [2]. See also [1] for a comparison with the PACS scan map calibration.

### 5.1 Observations obtained between OD 300 and the end of operations

Measurements after OD 300 yield results according to the statistics shown in Tab. 3. Using those as a reference for comparing with the flux calibration based on scan maps, the measured source fluxes obtained from chop-nod observations are on average lower by 6.5%, 5.6% and 4.6% at 70, 100, and 160  $\mu\text{m}$ , respectively, with an uncertainty that is of the order of 2%. These numbers already provide reasonable flux correction factors for chop-nod observations obtained from OD 300 onwards.

Note that the quoted uncertainties of the individual objects only reflect the reproducibility of the photometry. The absolute calibration uncertainty is dominated by the model uncertainties that amount to 5%. For some of the objects, the uncertainties are higher than for the others, particularly at 160  $\mu\text{m}$ . To rule out intrinsic flux variations as the cause, we have analysed the correlation between the model flux and the rms of the individual object photometries. As shown in Fig. 5, the increased scatter of the photometry of  $\alpha$  Cet and  $\gamma$  Dra at 160  $\mu\text{m}$  anti-correlates with their model flux. In addition, the results of the scan-map observations have a higher fidelity and do not scatter that much [1]. Therefore, the obtained uncertainty is not due to real flux variations, but can be entirely explained by a reduced S/N of an individual measurement. This also demonstrates that for relatively faint objects a photometric error prediction is unreliable.

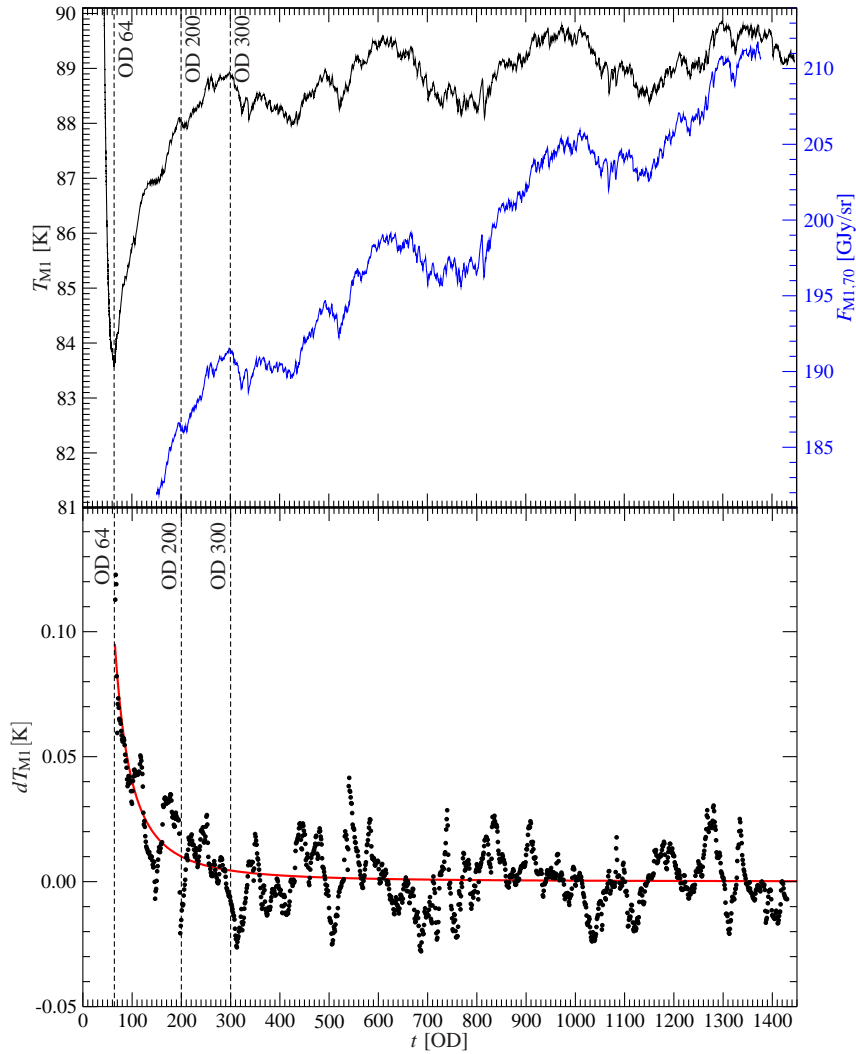


**Fig. 6** Evolution of the telescope main mirror temperature (black line, upper panel), of the modelled flux density at  $70 \mu\text{m}$  (blue line, upper panel) and of the first derivative of the telescope main mirror temperature (lower panel) during the Herschel mission. The solid red line is a fit to the data according to  $dT_{M1} = c \cdot t^{-2}$ .

## 5.2 Observations obtained until OD 300

The measured flux, at  $70 \mu\text{m}$  of the calibration objects declines nearly linearly until OD 300. The same is visible for the other two bands after normalising the individual sources to the same mean flux ratio distribution (see Fig. 10). For this, the data of each of the five objects have been divided by their individually derived mean flux ratios measured in a given wave band and then multiplied with the mean of the complete set of targets. It is interesting that such a behaviour is not seen for scan map

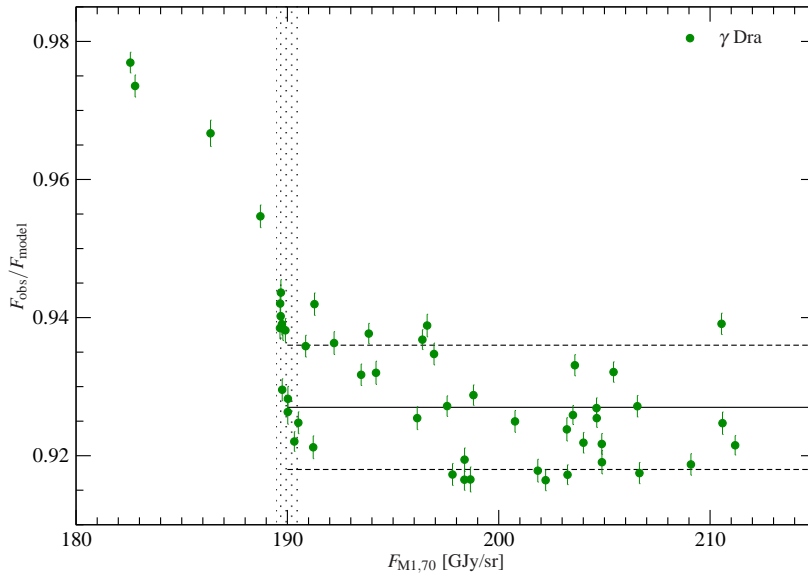


**Fig. 7** Photometric results of  $\gamma$  Dra vs. the corresponding modelled telescope main mirror flux at  $70 \mu\text{m}$ . The shaded area around  $190 \text{ GJy/sr}$  represents the range of telescope fluxes attained around OD 300. The horizontal lines represent the mean and the rms for ODs  $\geq 300$ . All the data points at lower flux values have been obtained on earlier ODs.

observations, but there were not many of such observations done during this period, either. Furthermore, this drift is not detected when analysing the signal of the internal calibration sources obtained during the calibration block measurements [7]. This points to an origin of the effect outside the PACS instrument.

The telescope main mirror is the by far brightest background emitter with an estimated mean flux of  $200$ ,  $145$  and  $95 \text{ GJy/sr}$  at  $70$ ,  $100$ , and  $160 \mu\text{m}$  (Poglitsch, priv. comm.) that determines the average thermal load on the detectors. It varies with time, mostly due to seasonal effects. The flux can be modelled by using the measured mirror temperature as an input and including certain assumptions for emissivity and its change during the Herschel mission. Figure 6 (upper panel) demonstrates how the mean temperature of the telescope main mirror and its modelled flux at  $70 \mu\text{m}$  varies with time. We see that after the initial cool-down phase until OD 64, there is a period of rapid warm-up until approximately OD 200.

The variation of the total flux load on the detectors modifies their response. A brighter background radiation leads to smaller measured point source fluxes. As shown in [1], some of the scatter produced by the photometry of the five standard stars observed with the scan map AOT can be mitigated, if the evolution of the telescope background flux is considered. To investigate the prospects of a similar correction for the chopped observations, we present Fig. 7, where the photometric results of  $\gamma$  Dra are put into perspective to the matching modelled telescope main mirror fluxes. Unfortunately, the temporal coverage of the model does not extend below OD 150, hence it misses most of the critical period, where the response deviated most. Therefore, we cannot trace the entire parameter space to look for a supposed correlation.

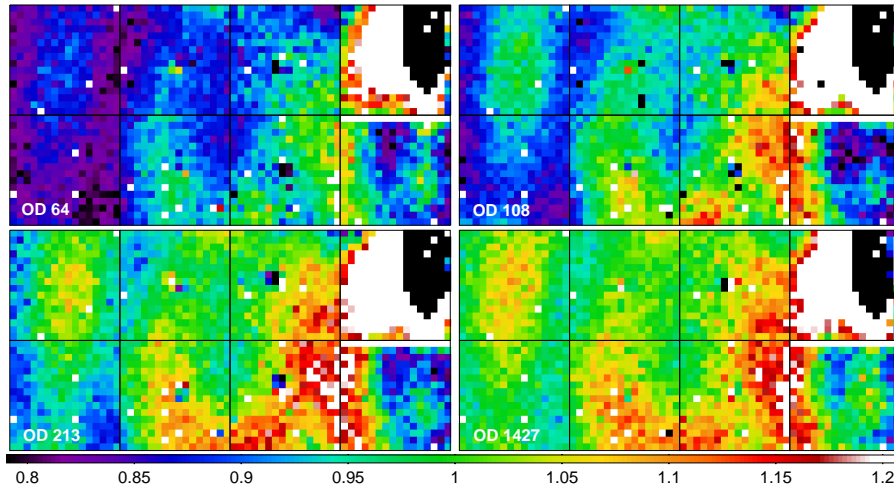


**Fig. 8** Visualisation of the differential signal variation of the short-wave detector array at  $70 \mu\text{m}$  caused by the changing telescope background for four ODs 64, 108, 213, 1427. The eight individual sub-matrices are indicated as black frames. The signals have been normalised to an observation obtained on OD 1444. While a similar emission patterns can be recognised in all of the four images, their scaling varies in time.

Nonetheless, the plot demonstrates that it is separated into two distinct populations. The intersection happens at a main mirror flux of around  $190 \text{ GJy/sr}$  at  $70 \mu\text{m}$ , which coincides with the period around OD 300. It seems that the short term variations and long term trend as of OD 300 of the chopped photometer data may also be corrected for influences by the changing main mirror flux, but not the strong decline in response at the beginning of the Herschel mission as visualised in Fig. 6 (lower panel). This effect seems to be caused by yet another phenomenon.

To find such influences, it is reasonable to look for causes that are related to the observing mode. The main difference to scan maps is the measurement at alternating ON and OFF positions during the chop-nod sequence. Chopping is done with a focal plane mirror that modifies the viewing angle by about  $50''$  along the instrument y-axis. To investigate a possible change in the differential signal that is produced by the chopping technique, we have produced images for chop-nod observations obtained at  $70 \mu\text{m}$ , where the chopped OFF position was subtracted from the chopped ON position. To be able to analyse the signal variation instead of the absolute signal, we have divided each image by the one derived from the last observation done on OD 1444 (see Eq. 1).

$$\frac{\langle \text{ON} - \text{OFF} \rangle_i}{\langle \text{ON} - \text{OFF} \rangle_{\text{OD1444}}} \quad (1)$$

The results for four observations from ODs 64, 108, 213 and 1427 are shown in Fig. 8. They demonstrate a clear change of the differential signal during the first phase of the Herschel mission. An even clearer picture of the evolution of the differential signal is given by Fig. 9. We have calculated the mean and the standard deviation of the normalised differential signals of all chopped  $\gamma$  Dra observations obtained at

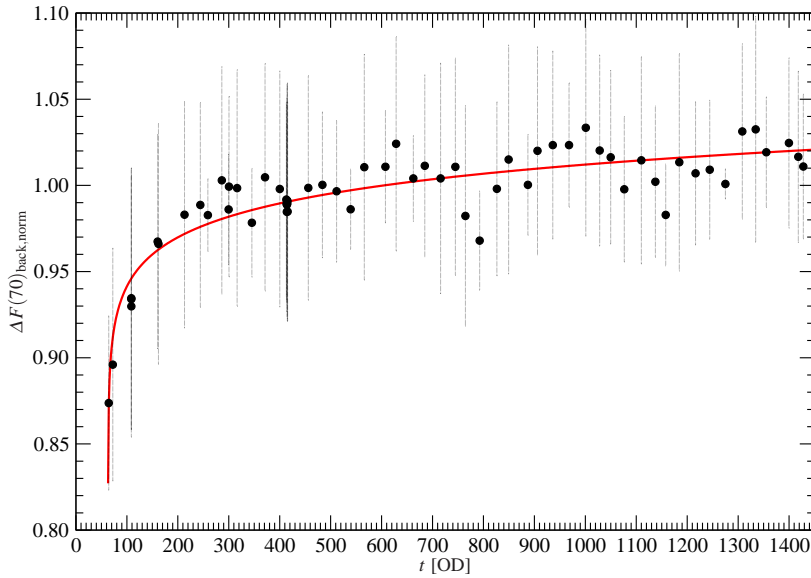


**Fig. 9** Evolution of the mean of the chopped differential background signal at  $70\ \mu\text{m}$  normalised to the results of the OD 1444 observation and measured by the two left detector matrices (see Fig. 8). The error bars represent the standard deviation of the signal distribution. The solid red line is a fit to the data according to  $\Delta F(70)_{\text{back, norm}} = c_1 \cdot (t - t_0)^{c_2} + c_3$ .

$70\ \mu\text{m}$  measured in the two left blue detector matrices (see Figs. 1, 8). This reflects the change of the differential background flux seen by the PACS instrument.

Such a change in the differential signal can only be explained by a stronger flux and temperature gradient between the two beams. A temperature gradient across the telescope main mirror does not explain this behaviour, because

1. the eight thermistors attached to it do not show any significant variation in the pairwise differences of the measured temperature,
2. the areas on the mirror covered by the alternating beams during chopping only deviate slightly. Even if the temperature of the main mirror had a strong spatial gradient, the effect would be quite small.

The strong temperature drift of the main mirror as shown in Fig. 6 (lower panel) and a similar behaviour of the secondary mirror suggest that the whole telescope was not yet thermally stable, as it was after OD 300, so that the alternating beam paths register a changing offset of the background flux. This appears to be the root cause for the response drift of the detectors we want to correct for.

This phenomenon is in so far quite striking, because it covers the PV phase, in which the final tuning and initial calibration of the detectors were supposed to happen. It seems that the conditions during that phase were not quite comparable to those experienced during the Routine Science Phase (RSP). Therefore, it is important to re-investigate the instrument calibration during the Post-Operations Phase (POP), when all long term effects can be analysed.

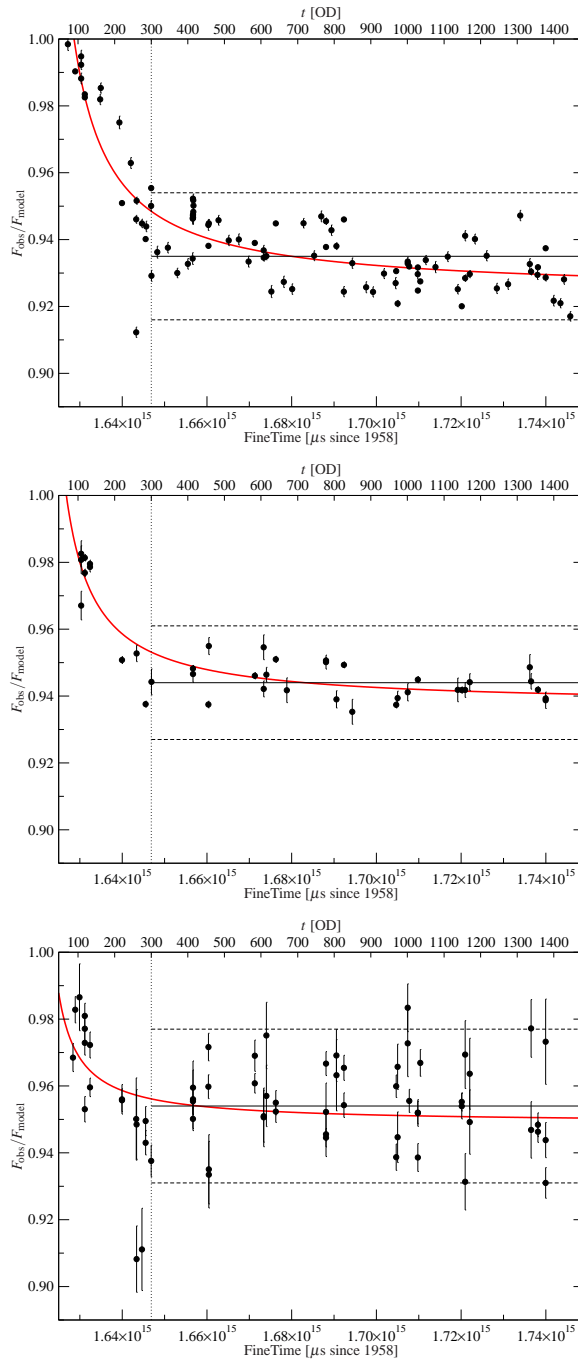


**Fig. 10** Photometric results of the measured calibration sources at 70, 100, and 160  $\mu\text{m}$  (top to bottom) vs. time normalised to the mean flux ratio in each band according to Tab. 3. The horizontal lines depict the mean and the rms of the averaged photometric results for  $\text{OD} \geq 300$  obtained for the three wave bands. The red lines correspond to the fits according to Eq. 2 and Tab. 4.

**Table 4** Fit parameters according to Eq. 2.

Wavelength	$c_1$	$c_2$	Uncertainty
70 $\mu\text{m}$	0.924	$6.551 \times 10^{-4}$	0.9%
100 $\mu\text{m}$	0.937	$4.276 \times 10^{-4}$	0.6%
160 $\mu\text{m}$	0.949	$1.948 \times 10^{-4}$	1.9%

## 6 Correction

The discovered variation of the differential background flux suggests a similar functional relationship of the response change with time instead of a simple and physically unjustified piecewise linear evolution. For now, we neglect a direct correlation between the response change and the variation of the background flux, mainly because the current telescope model is not the final one. This may be re-investigated in the near future. Instead, we empirically fit the data with a relationship that is motivated by this measurement.

Before being able to fit the photometric data, we first normalise them to their combined mean flux ratios of each wave band according to Tab. 3. The flux ratios of each of the objects are first divided by their mean and then multiplied by the global mean per wave band. In this way, we are able to merge the five individual datasets per wavelength into a single one, and at the same time, derive a result that is independent of the number of observations per target (see Fig. 10). We have removed the photometry of  $\gamma$  Dra from the fit at 160  $\mu\text{m}$  because of the large scatter (see Sect. 5.1). During the first attempts, we kept the exponent of the power-law fit as a free parameter. However, it turned out to be close to  $-1$  in all cases, so we decided to fix it to this value and fit only two parameters without affecting the reliability of the fit. Finally, the fits have been derived according to

$$\frac{F_{\text{obs}}}{F_{\text{model}}} = c_1 + c_2 \left( \frac{\text{FT}}{10^{15}} - 1.62 \right)^{-1} \quad (2)$$

where FT is the time in `FineTime` units. The values of the fitting parameters  $c_1$  and  $c_2$  are given in Tab. 4. The results are presented in Fig. 10.

The results show that the correction is most important for the 70  $\mu\text{m}$  band, while at 160  $\mu\text{m}$  it is only small, at least for the objects we include in our calibration. For higher S/N data, the effect may be more obvious. Table 4 together with Eq. 2 is used to calculate the flux correction to the data. This is done by determining a representative (the central) time of a given observation, express it in `FineTime` units and compute Eq. 2 for the suitable wavelength. For correcting the data, the signal values must be divided by the result.

In order to verify the correction derived by the method described above, we have applied it to the calibration observations. We modified the detector data directly by using the task definition provided in Sect. C.1. In order for it to work properly, it must be placed after the pipeline tasks `photRespFlatfieldCorrection` and `photNonLinearityCorrection`. However, the correction can also be done by applying it to the photometry results.

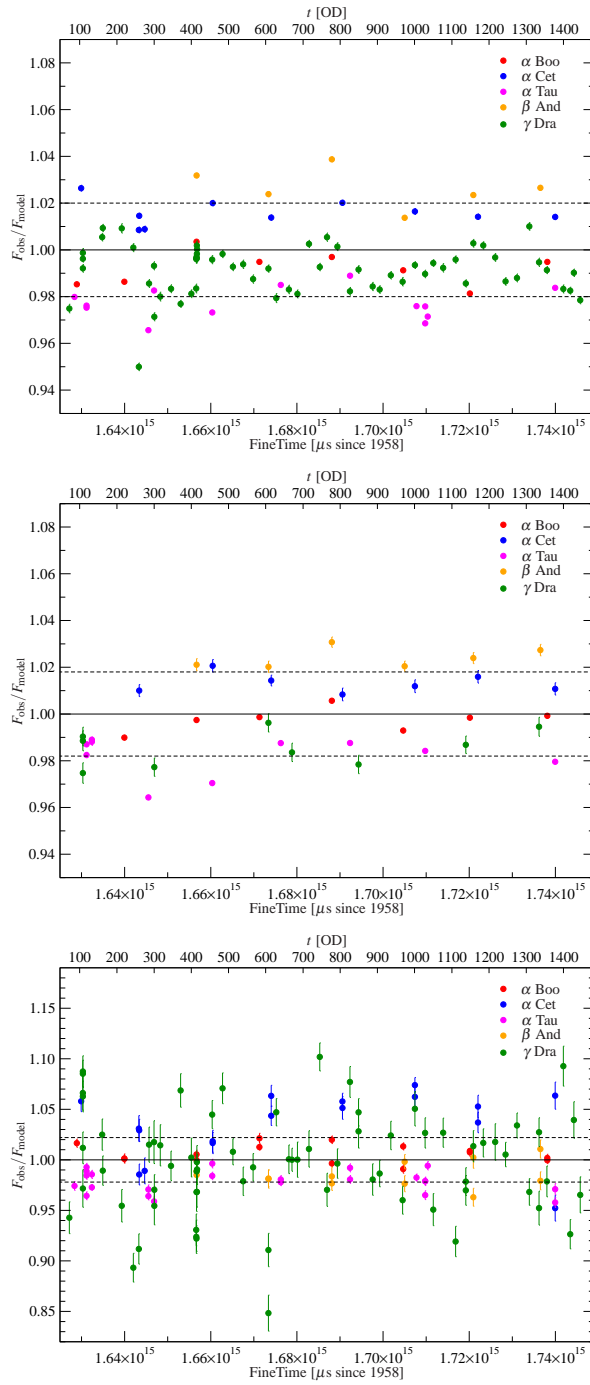


**Fig. 11** Photometric results of the measured calibration sources at 70, 100, and 160  $\mu\text{m}$  (top to bottom) vs. time after applying the calibration correction. The horizontal lines depict the mean and the rms derived from the averaged photometric results of the individual objects.



**Table 5** Results of the photometry of the five prime standard stars after applying the flux calibration correction. The quoted numbers are the mean values of the flux ratios of all observations. When combining more than one object, the mean is weighted by the number of objects.

Object(s)	70 $\mu\text{m}$	$\langle F_{\text{obs}}/F_{\text{model}} \rangle$ 100 $\mu\text{m}$	160 $\mu\text{m}$
$\alpha$ Boo	$0.992 \pm 0.007$	$0.997 \pm 0.005$	$1.006 \pm 0.009$
$\alpha$ Cet	$1.016 \pm 0.005$	$1.013 \pm 0.004$	$1.034 \pm 0.033$
$\alpha$ Tau	$0.977 \pm 0.007$	$0.982 \pm 0.008$	$0.978 \pm 0.011$
$\beta$ And	$1.026 \pm 0.008$	$1.024 \pm 0.004$	$0.986 \pm 0.013$
$\gamma$ Dra	$0.991 \pm 0.010$	$0.986 \pm 0.008$	$0.997 \pm 0.051$
K giants	$0.987 \pm 0.008$	$0.988 \pm 0.008$	$0.994 \pm 0.014$
M giants	$1.021 \pm 0.008$	$1.019 \pm 0.008$	$1.010 \pm 0.035$
all	$1.000 \pm 0.020$	$1.000 \pm 0.018$	$1.000 \pm 0.022$

The new photometric results after applying the flux correction are shown in Fig. 11. The statistics are summarised in Tab. 5. In addition, the corrected flux values of all observations are listed in Tab. 7. The main results are that

- the mean ratio between the model and the measured flux is 1 when weighting the data according to the mean of the individual targets,
- the initial response change has disappeared.

One might get the impression that the data have been slightly over-corrected at 100  $\mu\text{m}$ , but this is caused by the low number statistics, the lower S/N of the fainter objects and the spread among the individual objects. Note that the horizontal lines in the plots representing the mean and rms are derived from the mean values calculated for a given target. The rms does not reflect the reproducibility of the photometry, which itself is of the order of 1%, if the S/N is high enough (see Tab. 5).

## 7 Discussion and Caveats

### 7.1 Model fluxes

The stellar spectra have been modelled by assuming for each star a constant stellar radius for all wavelengths. A correct modelling would have to include optical depth effects that are wavelength dependent and result in varying effective stellar radii. Correcting for this effect would introduce flux changes of the order of 2%. This will be included in future flux calibrations.

### 7.2 Empirical approach

Although the flux correction is motivated by a physical change of the measured differential background flux that is most likely responsible for the response drift at the beginning of the Herschel mission, the correction itself is a pure empirical approach

with some ad hoc assumptions. In particular, the origin of the scaling factor between chop-nod and scan map observations beyond OD 300 is not fully understood, although it is believed that to some extent the different signal modulation frequencies play a role. Nevertheless, we are certain that the flux correction as derived here is reliable and at least reduces the systematic uncertainties due to the mismatch introduced by the scan-map-based flux calibration. The PACS Instrument Control Centre (ICC) is working on deriving a realistic time-dependent flux model of the telescope main mirror that may help to re-iterate on this issue in the future.

### 7.3 Aperture correction

The aperture correction applied to the photometry is based on an encircled energy function of a template PSF that was derived from scan map observations. We already know that the PSF derived from scan map observations is not even universal for all types of scan maps, let alone can it be regarded as a good representation of the PSF produced by chop-nod observations. However, the differences are small and mostly affect the wings. Therefore, by selecting a large aperture, the uncertainties introduced by the aperture correction are minimised. The remaining systematic differences are contained in the flux correction factors.

Theoretically, one would have to derive proper PSFs from point source observations using the chopped photometry AOT. However, this is compromised by a small effective field-of-view (FOV) in the maps, so that the PSFs of the neighbouring images (see Fig. 3) may prevent establishing a suitable template PSF from the central image (see also Sect. 7.4).

### 7.4 Flux dependency

At the moment, the flux correction for chop-nod observations has only been verified for a restricted range of source fluxes, i. e. the prime calibrators. Further systematic verifications using much brighter objects (e. g. planets, asteroids) is still an outstanding issue. First tests seem to confirm that such a flux dependency might be negligible [8].

One possible source of introducing such a suggested flux dependency is the limited FOV of the point-source maps. The patches in the map belonging to the individual positive and negative images of the object are smaller than their measurable PSF. This potentially can lead to a contamination of the background level of the central patch that is used for the photometry. Such a contamination may depend on the brightness of a given object. For rather faint objects, the PSF declines quickly enough so that contributions from the surrounding images to the central image are well below the noise level. This is not the case for very bright objects or high S/N data. The potential amount of contamination is yet to be established.

## 8 Conclusions

We have presented a reliable flux calibration for the chopped point-source photometry AOT observing mode of the PACS photometer on-board the Herschel Space Observatory, whose flux calibration is tuned to the preferred observing mode, i. e. scan maps. This was done by scaling the photometric results of the five PACS prime standard stars  $\alpha$  Boo,  $\alpha$  Cet,  $\alpha$  Tau,  $\beta$  And, and  $\gamma$  Dra obtained from chopped observations to the scan-map based calibration scheme.

We found a strong decline of the measured integrated point-source flux densities for the first 300 Operational Days that is not seen for scan map observations. If only the results beyond that threshold are considered, the photometry produces results that are on average lower by 5 – 6% than what is obtained from scan map observations. In addition, we find that the K and M giants in the sample produce slightly different results of the order 2 – 3% in all bands.

In an attempt to identify the reason for the initial rapid change of the effective signal response, we have found an equally strong variation of the measured differential background flux that indicates a systematic change of the temperature or flux gradient seen by the alternating instrument beam. This variation seems to be anti-correlated with the photometric results. It is known that a higher background flux reduces the response of the bolometers. The root cause that is responsible for changing the gradient in the background flux is unknown, but we were able to restrict it to an origin outside the PACS instrument.

After fitting an empirical relationship between the measured ratios of the model and photometric fluxes for every calibration object and in each band, the initial response drift has disappeared. In addition, the residual scatter of the modelled-to-measured flux ratios of the five calibrators are consistent within 2%, which is well below the quoted model uncertainty of 5%. The reproducibility for a given object is of the order 1% at 70 and 100  $\mu\text{m}$  and varies between 1% and 5% at 160  $\mu\text{m}$ . The latter can be explained by a decreasing signal-to-noise ratio.

This demonstrates the reliability of the established flux calibration that is of the same order as achieved for the scan map observing mode.

**Acknowledgements** We thank the anonymous referee for the constructive report on the submitted manuscript. We also would like to thank J. Blommaert (KUL) for providing helpful comments. Z. Balog, H. Linz and M. Nielbock are funded by the Deutsches Zentrum für Luft- und Raumfahrt e. V.

## References

1. Balog, Z., Müller, T., Nielbock, M., Altieri, B., Klaas, U., Blommaert, J., Linz, H., Lutz, D., Moór, A., Billot, N., Sauvage, M., Okumura, K.: The Herschel-PACS photometer calibration: Point-source flux calibration. *Experimental Astronomy* **this issue**, submitted (2013)
2. Dehaes, S., Bauwens, E., Decin, L., Eriksson, K., Raskin, G., Butler, B., Dowell, C.D., Ali, B., Blommaert, J.A.D.L.: Structure of the outer layers of cool standard stars. *Astronomy & Astrophysics* **533**, A107 (2011). DOI 10.1051/0004-6361/200912442
3. Emerson, J.P.: Observing far-infrared and submillimeter continuum emission. In: T.P. Ray, S.V.W. Beckwith (eds.) *Star Formation and Techniques in Infrared and mm-Wave Astronomy, Lecture Notes in Physics, Berlin Springer Verlag*, vol. 431, pp. 125–156 (1994). DOI 10.1007/3-540-58196-0\_33

4. Krause, O., Lemke, D., Grözinger, U., Böhm, A., Baumeister, H., Rohloff, R.R.: Cold focal plane chopper for the PACS instrument of the FIRST satellite: tests of an advanced prototype. In: M. Strojnik, B.F. Andresen (eds.) *Infrared Spaceborne Remote Sensing VIII, Society of Photo-Optical Instrumentation Engineers (SPIE) Conference Series*, vol. 4131, pp. 120–131 (2000)
5. Lagage, P.O., Durand, G.A., Lyraud, C., Rio, Y., Pel, J.W., de Haas, J.C.: Final design of VISIR: the mid-infrared imager and spectrometer for the VLT. In: M. Iye, A.F. Moorwood (eds.) *Optical and IR Telescope Instrumentation and Detectors, Society of Photo-Optical Instrumentation Engineers (SPIE) Conference Series*, vol. 4008, pp. 1120–1131 (2000)
6. Lemke, D., Garzon, F., Gemuend, H.P., Groezinger, U., Heinrichsen, I., Klaas, U., Kraetschmer, W., Kreysa, E., Luetzow-Wentzky, P., Schubert, J., Wells, M., Wolf, J.: ISOPHOT: far-infrared imaging, polarimetry, and spectrophotometry on ISO. In: M.S. Scholl (ed.) *Infrared Spaceborne Remote Sensing, Society of Photo-Optical Instrumentation Engineers (SPIE) Conference Series*, vol. 2019, pp. 28–33 (1993)
7. Moór, A., Müller, T., Kiss, C., Balog, Z., Marton, G.: PACS photometer calibration block analysis. *Experimental Astronomy* **this issue**, submitted (2013)
8. Müller, T., Balog, Z., Nielbock, M., Lim, T., Teyssier, D., Olberg, M., Klaas, U.: Herschel celestial calibration sources: Four large main-belt asteroids as prime flux calibrators. *Experimental Astronomy* **this issue**, submitted (2013)
9. Ott, S.: The Herschel Data Processing System – HIPE and Pipelines – Up and Running Since the Start of the Mission. In: Y. Mizumoto, K.I. Morita, M. Ohishi (eds.) *Astronomical Data Analysis Software and Systems XIX, Astronomical Society of the Pacific Conference Series*, vol. 434, p. 139 (2010)
10. Pilbratt, G.L., Riedinger, J.R., Passvogel, T., Crone, G., Doyle, D., Gageur, U., Heras, A.M., Jewell, C., Metcalfe, L., Ott, S., Schmidt, M.: Herschel Space Observatory. An ESA facility for far-infrared and submillimetre astronomy. *Astronomy & Astrophysics* **518**, L1 (2010). DOI 10.1051/0004-6361/201014759
11. Poglitsch, A., Waelkens, C., Geis, N., Feuchtgruber, H., Vandenbussche, B., Rodriguez, L., Krause, O., Renotte, E., van Hoof, C., Saraceno, P., Cepa, J., Kerschbaum, F., Agnèse, P., Ali, B., Altieri, B., Andreani, P., Augeres, J.L., Balog, Z., Barl, L., Bauer, O.H., Belbachir, N., Benedettini, M., Billot, N., Boulade, O., Bischof, H., Blommaert, J., Callut, E., Cara, C., Cerulli, R., Cesarsky, D., Contursi, A., Creten, Y., De Meester, W., Doublier, V., Doumayrou, E., Duband, L., Exter, K., Genzel, R., Gillis, J.M., Grözinger, U., Henning, T., Herreros, J., Huygen, R., Inguscio, M., Jakob, G., Jamar, C., Jean, C., de Jong, J., Katterloher, R., Kiss, C., Klaas, U., Lemke, D., Lutz, D., Madden, S., Marquet, B., Martignac, J., Mazy, A., Merken, P., Montfort, F., Morbidelli, L., Müller, T., Nielbock, M., Okumura, K., Orfei, R., Ottensamer, R., Pezzuto, S., Popesso, P., Putzeys, J., Regibo, S., Reveret, V., Royer, P., Sauvage, M., Schreiber, J., Stegmaier, J., Schmitt, D., Schubert, J., Sturm, E., Thiel, M., Tofani, G., Vavrek, R., Wetzstein, M., Wieprecht, E., Wiezorrek, E.: The Photodetector Array Camera and Spectrometer (PACS) on the Herschel Space Observatory. *Astronomy & Astrophysics* **518**, L2 (2010). DOI 10.1051/0004-6361/201014535
12. Reimann, H.G., Linz, H., Wagner, R., Relke, H., Kaeufl, H.U., Dietzsch, E., Sperl, M., Hron, J.: TIMM2: a new multimode mid-infrared instrument for the ESO 3.6-m telescope. In: M. Iye, A.F. Moorwood (eds.) *Optical and IR Telescope Instrumentation and Detectors, Society of Photo-Optical Instrumentation Engineers (SPIE) Conference Series*, vol. 4008, pp. 1132–1143 (2000)
13. van Leeuwen, F.: Validation of the new Hipparcos reduction. *Astronomy & Astrophysics* **474**, 653–664 (2007). DOI 10.1051/0004-6361:20078357
14. Wieprecht, E., Schreiber, J., de Jong, J., Jacobson, J., Liu, C., Morien, B., Wetzstein, M., Ali, B., Frayer, D., Lutz, D., Okumura, K., Popesso, P., Sauvage, M.: The Herschel/Pacs Photometer Pipeline. In: D.A. Bohlender, D. Durand, P. Dowler (eds.) *Astronomical Data Analysis Software and Systems XVIII, Astronomical Society of the Pacific Conference Series*, vol. 411, p. 531 (2009)

## A List of Observations

**Table 6** List of observations. The repetition factor was always set to 1. The first four observations and the one with OBSID 1342184286 were carried out with low gain settings. This had no influence on the photometry.

OD	OBSID	AOR label
72	1342180683	PVPhotFPG_261C_StdPS_blu_SAA-20-10_HIP87833
86	1342181662	PVPhotFPG_261F_StdPS_blu_SAA+20+30_HIP21421_0001
92	1342182100	PVPhotFPG_261G_StdPS_blu_SAA_0+30_HIP69673_OD92_01
104	1342182830	PVPhotFPG_261C_PS_blu_SAA-20-10_HIP14135_OD104_01
108	1342182990	PVPhotAOTVal_511A_StdPSdith_blu_gammaDra_0001
108	1342182991	PVPhotAOTVal_511A_StdPSndith_blu_gammaDra_0001
108	1342182993	PVPhotFlux_321C_StdPS_photcal_blu_gammaDra_0001
108	1342182994	PVPhotAOTVal_511A_StdPSndith_grn_gammaDra_0001
108	1342182995	PVPhotFlux_321C_StdPS_photcal_grn_gammaDra_0001
108	1342182996	PVPhotAOTVal_511A_StdPSdith_grn_gammaDra_0001
118	1342183530	PVPhotFlux_321C_StdPS_photcal_blu_alfTau_0001
118	1342183531	PVPhotFlux_321C_StdPS_photcal_grn_alfTau_0001
118	1342183536	PVPhotSpatial_314B_StdPSdith_blu_alfTau_0001
118	1342183537	PVPhotSpatial_314B_StdPSdith_grn_alfTau_0001
132	1342184285	PVPhotFlux_324A_StdPS_hi10Jy_grn_alfTau_0002
132	1342184286	PVPhotFlux_323A_StdPS_lo10Jy_grn_alfTau_0002
160	1342186140	PVPhotFlux_321B_StdPS_photcal_blu_gamDra_0001
161	1342186191	PVPhotFlux_321B_StdPS_photcal_blu_gamDra_0002
213	1342188069	RPPhotFlux_321A_cPS_repro_blu_gamDra_0001
220	1342188243	RPPhotFlux_321C_cPS_photcal_blu_alfBoo_0001
220	1342188244	RPPhotFlux_321C_cPS_photcal_grn_alfBoo_0001
244	1342189188	RPPhotFlux_321A_cPS_repro_blu_gamDra_0002
258	1342189775	RPPhotFPG_261A_StdPS_blu_SAA-20+30_OD258_HIP87833
258	1342189783	RPPhotFPG_261A_StdPS_blu_SAA-20+30_OD258_HIP14135
259	1342189823	RPPhotFlux_321C_cPS_photcal_blu_alfCet_0001
259	1342189826	RPPhotFlux_321C_cPS_photcal_grn_alfCet_0001
274	1342190603	RPPhotFPG_261A_cPS_blu_SAA-20+30_OD274_ni_HIP14135
284	1342190943	RPPhotFlux_324A_cPS_10Jy_grn_alfTau_0001
284	1342190946	RPPhotFlux_324A_cPS_20Jy_blu_alfTau_0001
286	1342191124	RPPhotFlux_321A_cPS_repro_blu_gamDra_0003
299	1342191848	RPPhotFPG_261B_cPS_blu_SAA-20+30_OD299_ni_HIP87833
299	1342191870	RPPhotFPG_261B_cPS_blu_SAA-20+30_OD299_ni_HIP21421
300	1342191957	RPPhotFlux_321A_cPS_repro_blu_gamDra_0004
300	1342191960	RPPhotFlux_324A_cPS_2Jy_grn_gamDra_0001
316	1342192779	RPPhotFlux_321A_cPS_repro_blu_gamDra_0005
345	1342195482	RPPhotFlux_321A_cPS_repro_blu_gamDra_0006
371	1342196729	RPPhotFlux_321A_cPS_repro_blu_gamDra_0007
400	1342198498	RPPhotFlux_321A_cPS_repro_blu_gamDra_0008
413	1342199480	RPPhotFlux_321A_cPS_repro_blu_gamDra_0009
413	1342199511	RPPhotFlux_321A_cPS_repro_blu_gamDra_0010
413	1342199525	RPPhotFlux_321A_cPS_repro_blu_gamDra_0011
414	1342199599	RPPhotFlux_321A_cPS_repro_blu_gamDra_0012
414	1342199602	RPPhotFlux_324A_cPS_20Jy_blu_alfBoo_0001
414	1342199605	RPPhotFlux_324A_cPS_10Jy_grn_alfBoo_0001
414	1342199608	RPPhotFlux_321C_cPS_photcal_blu_betAnd_0001
414	1342199611	RPPhotFlux_321C_cPS_photcal_grn_betAnd_0001
414	1342199638	RPPhotFlux_321A_cPS_repro_blu_gamDra_0013

Table 6 continued.

OD	OBSID	AOR label
414	1342199654	RPPhotFlux_321A_cPS_repro_blu_gamDra_0014
415	1342199706	RPPhotFlux_321A_cPS_repro_blu_gamDra_0015
415	1342199716	RPPhotFlux_321A_cPS_repro_blu_gamDra_0016
456	1342202941	RPPhotFlux_321A_cPS_repro_blu_gamDra_0018
456	1342202957	RPPhotFlux_324A_cPS_10Jy_grn_alfTau_0002
456	1342202960	RPPhotFlux_324A_cPS_20Jy_blu_alfTau_0002
457	1342203029	RPPhotFlux_324A_cPS_5Jy_blu_alfCet_0001
457	1342203032	RPPhotFlux_324A_cPS_2Jy_grn_alfCet_0001
483	1342204208	RPPhotFlux_321A_cPS_repro_blu_gamDra_0019
511	1342206000	RPPhotFlux_321A_cPS_repro_blu_gamDra_0020
539	1342208970	RPPhotFlux_321A_cPS_repro_blu_gamDra_0021
566	1342210581	RPPhotFlux_321A_cPS_repro_blu_gamDra_0022
583	1342211279	RPPhotFlux_324A_cPS_20Jy_blu_alfBoo_0002
583	1342211282	RPPhotFlux_324A_cPS_10Jy_grn_alfBoo_0002
607	1342212493	RPPhotFlux_321A_cPS_repro_blu_gamDra_0023
607	1342212496	RPPhotFlux_324A_cPS_2Jy_grn_gamDra_0002
607	1342212503	RPPhotFlux_324A_cPS_2Jy_grn_betaAnd_0001
607	1342212506	RPPhotFlux_324A_cPS_5Jy_blu_betaAnd_0001
614	1342212852	RPPhotFlux_324A_cPS_2Jy_grn_alfCet_0002
614	1342212855	RPPhotFlux_324A_cPS_5Jy_blu_alfCet_0002
628	1342213587	RPPhotFlux_321A_cPS_repro_blu_gamDra_0024
640	1342214210	RPPhotFlux_324A_cPS_20Jy_blu_alfTau_0003
640	1342214213	RPPhotFlux_324A_cPS_10Jy_grn_alfTau_0003
662	1342215373	RPPhotFlux_321A_cPS_repro_blu_gamDra_0025
670	1342216068	RPPhotFlux_324A_cPS_2Jy_grn_gamDra_0003
684	1342217403	RPPhotFlux_321A_cPS_repro_blu_gamDra_0026
715	1342220822	RPPhotFlux_321A_cPS_repro_blu_gamDra_0027
744	1342221810	RPPhotFlux_321A_cPS_repro_blu_gamDra_0028
764	1342222755	RPPhotFlux_321A_cPS_repro_blu_gamDra_0029
777	1342223334	RPPhotFlux_324A_cPS_5Jy_blu_betaAnd_0003
777	1342223337	RPPhotFlux_324A_cPS_2Jy_grn_betaAnd_0003
777	1342223344	RPPhotFlux_324A_cPS_20Jy_blu_alfBoo_0003
777	1342223347	RPPhotFlux_324A_cPS_10Jy_grn_alfBoo_0003
792	1342224228	RPPhotFlux_321A_cPS_repro_blu_gamDra_0030
806	1342224926	RPPhotFlux_324A_cPS_5Jy_blu_alfCet_0003
806	1342224929	RPPhotFlux_324A_cPS_2Jy_grn_alfCet_0003
826	1342226711	RPPhotFlux_321A_cPS_repro_blu_gamDra_0031
826	1342226739	RPPhotFlux_324A_cPS_20Jy_blu_alfTau_0004
826	1342226742	RPPhotFlux_324A_cPS_10Jy_grn_alfTau_0004
849	1342228387	RPPhotFlux_321A_cPS_repro_blu_gamDra_0032
849	1342228390	RPPhotFlux_324A_cPS_2Jy_grn_gamDra_0004
887	1342231096	RPPhotFlux_321A_cPS_repro_blu_gamDra_0033
906	1342231898	RPPhotFlux_321A_cPS_repro_blu_gamDra_0034
936	1342234213	RPPhotFlux_321A_cPS_repro_blu_gamDra_0035
967	1342237974	RPPhotFlux_321A_cPS_repro_blu_gamDra_0036
969	1342236964	RPPhotFlux_324A_cPS_10Jy_grn_alfBoo_0004
969	1342236967	RPPhotFlux_324A_cPS_20Jy_blu_alfBoo_0004
973	1342237160	RPPhotFlux_324A_cPS_2Jy_grn_betaAnd_0004
973	1342237163	RPPhotFlux_324A_cPS_5Jy_blu_betaAnd_0004
1000	1342238771	RPPhotFlux_321A_cPS_repro_blu_gamDra_0037
1000	1342238778	RPPhotFlux_324A_cPS_2Jy_grn_alfCet_0004
1000	1342238781	RPPhotFlux_324A_cPS_5Jy_blu_alfCet_0004
1005	1342239042	ObsCal_RP_FPG_PPhot_Blue_cycle59_OD1005_HIP21421
1028	1342240698	RPPhotFlux_321A_cPS_repro_blu_gamDra_0038

Table 6 continued.

OD	OBSID	AOR label
1028	1342240753	ObsCal_RP_FPG_PPhot_Blue_cycle60_OD1028_HIP21421
1028	1342240754	RPPhotFlux_324A_cPS_20Jy_blu_alfTau_0005
1028	1342240757	RPPhotFlux_324A_cPS_10Jy_grn_alfTau_0005
1034	1342241329	ObsCal_RP_FPG_PPhot_Blue_cycle61_OD1034_HIP21421
1049	1342242556	RPPhotFlux_321A_cPS_repro_blu_gamDra_0039
1076	1342244899	RPPhotFlux_321A_cPS_repro_blu_gamDra_0040
1109	1342246180	RPPhotFlux_321A_cPS_repro_blu_gamDra_0041
1137	1342247334	RPPhotFlux_321A_cPS_repro_blu_gamDra_0042
1137	1342247337	RPPhotFlux_324A_cPS_2Jy_grn_gamDra_0005
1148	1342247701	RPPhotFlux_324A_cPS_10Jy_grn_alfBoo_0005
1148	1342247704	RPPhotFlux_324A_cPS_20Jy_blu_alfBoo_0005
1157	1342248031	RPPhotFlux_324A_cPS_2Jy_grn_betaAnd_0005
1157	1342248034	RPPhotFlux_324A_cPS_5Jy_blu_betaAnd_0005
1157	1342248037	RPPhotFlux_321A_cPS_repro_blu_gamDra_0043
1170	1342248718	RPPhotFlux_324A_cPS_2Jy_grn_alfCet_0005
1170	1342248721	RPPhotFlux_324A_cPS_5Jy_blu_alfCet_0005
1184	1342249292	RPPhotFlux_321A_cPS_repro_blu_gamDra_0044
1216	1342250855	RPPhotFlux_321A_cPS_repro_blu_gamDra_0045
1244	1342252804	RPPhotFlux_321A_cPS_repro_blu_gamDra_0046
1275	1342254722	RPPhotFlux_321A_cPS_repro_blu_gamDra_0047
1308	1342256958	RPPhotFlux_321A_cPS_repro_blu_gamDra_0048
1334	1342258830	RPPhotFlux_321A_cPS_repro_blu_gamDra_0049
1334	1342258833	RPPhotFlux_324A_cPS_2Jy_grn_gamDra_0006
1337	1342259256	RPPhotFlux_324A_cPS_2Jy_grn_betaAnd_0006
1337	1342259259	RPPhotFlux_324A_cPS_5Jy_blu_betaAnd_0006
1355	1342262224	RPPhotFlux_321A_cPS_repro_blu_gamDra_0050
1356	1342262515	RPPhotFlux_324A_cPS_10Jy_grn_alfBoo_0006
1356	1342262518	RPPhotFlux_324A_cPS_20Jy_blu_alfBoo_0006
1377	1342263906	RPPhotFlux_324A_cPS_2Jy_grn_alfCet_0006
1377	1342263909	RPPhotFlux_324A_cPS_5Jy_blu_alfCet_0006
1377	1342263914	RPPhotFlux_324A_cPS_10Jy_grn_alfTau_0006
1377	1342263917	RPPhotFlux_324A_cPS_20Jy_blu_alfTau_0006
1399	1342267290	RPPhotFlux_321A_cPS_repro_blu_gamDra_0051
1418	1342268965	RPPhotFlux_321A_cPS_repro_blu_gamDra_0052
1427	1342269811	RPPhotFlux_321A_cPS_repro_blu_gamDra_0053
1444	1342270999	RPPhotFlux_321A_cPS_repro_blu_gamDra_0054

## B Photometry of Observations

**Table 7** Photometry of all calibration observations.

OBSID	Object	Measured flux with correction applied [Jy]					
		$F_{70}$	$\sigma_{70}$	$F_{100}$	$\sigma_{100}$	$F_{160}$	$\sigma_{160}$
1342182100	$\alpha$ Boo	15.207	0.047			2.939	0.092
1342188243	$\alpha$ Boo	15.224	0.036			2.895	0.104
1342188244	$\alpha$ Boo			7.433	0.033	2.894	0.080
1342199602	$\alpha$ Boo	15.488	0.045			2.907	0.093
1342199605	$\alpha$ Boo			7.490	0.031	2.891	0.083
1342211279	$\alpha$ Boo	15.355	0.049			2.927	0.069
1342211282	$\alpha$ Boo			7.499	0.032	2.953	0.111
1342223344	$\alpha$ Boo	15.387	0.052			2.881	0.065
1342223347	$\alpha$ Boo			7.552	0.027	2.948	0.085
1342236964	$\alpha$ Boo			7.456	0.032	2.929	0.080
1342236967	$\alpha$ Boo	15.299	0.044			2.865	0.094
1342247701	$\alpha$ Boo			7.497	0.031	2.916	0.065
1342247704	$\alpha$ Boo	15.146	0.046			2.912	0.090
1342262515	$\alpha$ Boo			7.503	0.030	2.890	0.075
1342262518	$\alpha$ Boo	15.354	0.046			2.896	0.084
1342182830	$\alpha$ Cet	5.018	0.039			0.982	0.075
1342189783	$\alpha$ Cet	4.931	0.039			0.957	0.093
1342189823	$\alpha$ Cet	4.960	0.035			0.915	0.075
1342189826	$\alpha$ Cet			2.417	0.026	0.955	0.079
1342190603	$\alpha$ Cet	4.932	0.041			0.918	0.093
1342203029	$\alpha$ Cet	4.987	0.036			0.943	0.076
1342203032	$\alpha$ Cet			2.442	0.027	0.945	0.079
1342212852	$\alpha$ Cet			2.427	0.023	0.968	0.070
1342212855	$\alpha$ Cet	4.957	0.036			0.987	0.076
1342224926	$\alpha$ Cet	4.988	0.034			0.982	0.059
1342224929	$\alpha$ Cet			2.413	0.028	0.976	0.081
1342238778	$\alpha$ Cet			2.421	0.028	0.997	0.054
1342238781	$\alpha$ Cet	4.969	0.038			0.986	0.076
1342248718	$\alpha$ Cet			2.431	0.027	0.962	0.073
1342248721	$\alpha$ Cet	4.958	0.036			0.977	0.081
1342263906	$\alpha$ Cet			2.419	0.026	0.884	0.093
1342263909	$\alpha$ Cet	4.958	0.035			0.987	0.097
1342181662	$\alpha$ Tau	13.846	0.041			2.608	0.090
1342183530	$\alpha$ Tau	13.794	0.044			2.657	0.081
1342183531	$\alpha$ Tau			6.788	0.033	2.647	0.076
1342183536	$\alpha$ Tau	13.782	0.038			2.636	0.079
1342183537	$\alpha$ Tau			6.819	0.029	2.582	0.083
1342184285	$\alpha$ Tau			6.833	0.033	2.604	0.060
1342184286	$\alpha$ Tau			6.827	0.044	2.639	0.084
1342190943	$\alpha$ Tau			6.662	0.028	2.599	0.095
1342190946	$\alpha$ Tau	13.645	0.040			2.581	0.079
1342191870	$\alpha$ Tau	13.885	0.047			2.567	0.103
1342202957	$\alpha$ Tau			6.705	0.031	2.634	0.078
1342202960	$\alpha$ Tau	13.753	0.048			2.667	0.090
1342214210	$\alpha$ Tau	13.919	0.053			2.618	0.071
1342214213	$\alpha$ Tau			6.823	0.028	2.625	0.080



Table 7 continued.

OBSID	Object	Measured flux with correction applied [Jy]					
		$F_{70}$	$\sigma_{70}$	$F_{100}$	$\sigma_{100}$	$F_{160}$	$\sigma_{160}$
1342226739	$\alpha$ Tau	13.975	0.049			2.656	0.082
1342226742	$\alpha$ Tau			6.823	0.027	2.625	0.081
1342239042	$\alpha$ Tau	13.791	0.048			2.630	0.076
1342240753	$\alpha$ Tau	13.687	0.040			2.620	0.074
1342240754	$\alpha$ Tau	13.789	0.049			2.620	0.087
1342240757	$\alpha$ Tau			6.800	0.029	2.583	0.092
1342241329	$\alpha$ Tau	13.728	0.047			2.661	0.088
1342263914	$\alpha$ Tau			6.768	0.027	2.564	0.101
1342263917	$\alpha$ Tau	13.901	0.045			2.599	0.116
1342199608	$\beta$ And	5.772	0.035			1.050	0.069
1342199611	$\beta$ And			2.795	0.030	1.046	0.076
1342212503	$\beta$ And			2.792	0.029	1.042	0.077
1342212506	$\beta$ And	5.727	0.040			1.042	0.068
1342223334	$\beta$ And	5.811	0.036			1.037	0.058
1342223337	$\beta$ And			2.821	0.025	1.045	0.075
1342237160	$\beta$ And			2.793	0.025	1.060	0.059
1342237163	$\beta$ And	5.671	0.037			1.037	0.066
1342248031	$\beta$ And			2.803	0.027	1.023	0.074
1342248034	$\beta$ And	5.725	0.037			1.064	0.089
1342259256	$\beta$ And			2.812	0.028	1.040	0.074
1342259259	$\beta$ And	5.743	0.037			1.073	0.075
1342180683	$\gamma$ Dra	3.201	0.039			0.585	0.076
1342182990	$\gamma$ Dra	3.271	0.030			0.675	0.075
1342182991	$\gamma$ Dra	3.279	0.039			0.628	0.076
1342182993	$\gamma$ Dra	3.257	0.034			0.660	0.074
1342182994	$\gamma$ Dra			1.589	0.027	0.603	0.090
1342182995	$\gamma$ Dra			1.563	0.030	0.662	0.083
1342182996	$\gamma$ Dra			1.586	0.029	0.674	0.065
1342186140	$\gamma$ Dra	3.301	0.034			0.636	0.075
1342186191	$\gamma$ Dra	3.314	0.032			0.614	0.070
1342188069	$\gamma$ Dra	3.313	0.041			0.593	0.078
1342189188	$\gamma$ Dra	3.286	0.036			0.555	0.069
1342189775	$\gamma$ Dra	3.119	0.034			0.566	0.073
1342191124	$\gamma$ Dra	3.236	0.034			0.630	0.084
1342191848	$\gamma$ Dra	3.261	0.036			0.632	0.103
1342191957	$\gamma$ Dra	3.189	0.036			0.593	0.091
1342191960	$\gamma$ Dra			1.568	0.027	0.603	0.073
1342192779	$\gamma$ Dra	3.217	0.039			0.630	0.099
1342195482	$\gamma$ Dra	3.228	0.035			0.617	0.071
1342196729	$\gamma$ Dra	3.207	0.031			0.664	0.080
1342198498	$\gamma$ Dra	3.221	0.035			0.622	0.093
1342199480	$\gamma$ Dra	3.229	0.039			0.578	0.076
1342199511	$\gamma$ Dra	3.270	0.038			0.574	0.080
1342199525	$\gamma$ Dra	3.271	0.038			0.573	0.061
1342199599	$\gamma$ Dra	3.273	0.035			0.601	0.093
1342199638	$\gamma$ Dra	3.271	0.035			0.614	0.055
1342199654	$\gamma$ Dra	3.289	0.041			0.620	0.080
1342199706	$\gamma$ Dra	3.277	0.033			0.601	0.073
1342199716	$\gamma$ Dra	3.284	0.033			0.615	0.072
1342202941	$\gamma$ Dra	3.269	0.036			0.649	0.068
1342204208	$\gamma$ Dra	3.277	0.033			0.665	0.074
1342206000	$\gamma$ Dra	3.259	0.034			0.626	0.062

Table 7 continued.

OBSID	Object	Measured flux with correction applied [Jy]					
		$F_{70}$	$\sigma_{70}$	$F_{100}$	$\sigma_{100}$	$F_{160}$	$\sigma_{160}$
1342208970	$\gamma$ Dra	3.263	0.037			0.608	0.068
1342210581	$\gamma$ Dra	3.242	0.037			0.616	0.066
1342212493	$\gamma$ Dra	3.257	0.033			0.527	0.086
1342212496	$\gamma$ Dra			1.598	0.027	0.566	0.080
1342213587	$\gamma$ Dra	3.215	0.040			0.650	0.066
1342215373	$\gamma$ Dra	3.227	0.038			0.621	0.069
1342216068	$\gamma$ Dra			1.578	0.027	0.621	0.055
1342217403	$\gamma$ Dra	3.221	0.036			0.621	0.085
1342220822	$\gamma$ Dra	3.291	0.032			0.628	0.087
1342221810	$\gamma$ Dra	3.259	0.033			0.684	0.067
1342222755	$\gamma$ Dra	3.301	0.036			0.603	0.079
1342224228	$\gamma$ Dra	3.288	0.035			0.619	0.071
1342226711	$\gamma$ Dra	3.225	0.034			0.669	0.074
1342228387	$\gamma$ Dra	3.255	0.035			0.650	0.066
1342228390	$\gamma$ Dra			1.569	0.027	0.638	0.081
1342231096	$\gamma$ Dra	3.232	0.037			0.609	0.076
1342231898	$\gamma$ Dra	3.227	0.034			0.613	0.064
1342234213	$\gamma$ Dra	3.247	0.033			0.636	0.068
1342237974	$\gamma$ Dra	3.238	0.038			0.596	0.067
1342238771	$\gamma$ Dra	3.262	0.030			0.652	0.083
1342240698	$\gamma$ Dra	3.249	0.034			0.638	0.073
1342242556	$\gamma$ Dra	3.264	0.031			0.590	0.077
1342244899	$\gamma$ Dra	3.258	0.038			0.638	0.070
1342246180	$\gamma$ Dra	3.269	0.033			0.571	0.073
1342247334	$\gamma$ Dra	3.236	0.032			0.608	0.067
1342247337	$\gamma$ Dra			1.583	0.025	0.602	0.071
1342248037	$\gamma$ Dra	3.292	0.034			0.629	0.075
1342249292	$\gamma$ Dra	3.289	0.033			0.631	0.068
1342250855	$\gamma$ Dra	3.272	0.035			0.632	0.088
1342252804	$\gamma$ Dra	3.239	0.034			0.624	0.059
1342254722	$\gamma$ Dra	3.244	0.035			0.642	0.060
1342256958	$\gamma$ Dra	3.316	0.035			0.601	0.064
1342258830	$\gamma$ Dra	3.266	0.036			0.638	0.069
1342258833	$\gamma$ Dra			1.595	0.027	0.591	0.081
1342262224	$\gamma$ Dra	3.255	0.031			0.608	0.074
1342267290	$\gamma$ Dra	3.228	0.036			0.679	0.096
1342268965	$\gamma$ Dra	3.226	0.031			0.575	0.070
1342269811	$\gamma$ Dra	3.251	0.033			0.645	0.088
1342270999	$\gamma$ Dra	3.212	0.032			0.599	0.087

## C HIPE tasks

### C.1 Flux correction

```

"""
fluxCalCorrPs2Scan()
=====
This task scales the flux determined from aperture photometry of chopped PS
observations to the flux calibration scheme of scan maps. The conversion is
valid for integrated flux of up to approximately 10 Jy only.

Input parameters:
frames: the frames class
ft: time of the observation in FineTime
    (e.g. using getObstimeFromFrames)

Output parameters:
smframes: frames scaled to scan map flux scale
"""
def fluxCalCorrPs2Scan(frames,ft):
    pstosmcorr = TableDataset(description = "Chopped phot flux correction")
    pstosmcorr["Filter"]=Column(String1d(["blue","green","red"]))
    pstosmcorr["C1"]=Column(Double1d([0.924,0.937,0.949]))
    pstosmcorr["C2"]=Column(Double1d([6.551e-4,4.276e-4,1.948e-4]))

    smframes = frames.copy()
    if (smframes.meta["type"].value == "HPPAVGR"):
        filter = "red"
    elif (smframes.meta["blue"].value == "blue1"):
        filter = "blue"
    else:
        filter = "green"
    row = pstosmcorr["Filter"].data.where(pstosmcorr["Filter"].data ==
filter).toInt1d()
    c1 = pstosmcorr["C1"].data[row]
    c2 = pstosmcorr["C2"].data[row]
    corr = c1+c2/(ft.microsecondsSince1958()*1.0e-15-1.62)
    for i in range(smframes.getNumberOfFrames()):
        signal = smframes.refs[i].product["Signal"].data/corr
        smframes.refs[i].product["Signal"].data = signal
    pass
    return smframes

```

### C.2 Time of observation in FineTime

```

"""
getObstimeFromFrames()
=====
This task extracts the actual time at the middle of the observation. Start and
end times are extracted from level 0 detector data of the Observation Context.
The central time is returned as a FineTime.

Input parameter:
obs: Observation Context of the observation
"""
def getObstimeFromFrames(obs):
    frames = obs.level0.refs["HPPAVGB"].product
    framesStart = frames.getStartDate().microsecondsSince1958()
    framesEnd = frames.getEndDate().microsecondsSince1958()
    framesTime = (framesStart+framesEnd)/2
    ft=FineTime(framesTime)
    return ft

```